Optimized radiographic spectra for small animal digital subtraction angiography

Ming De Lin
Center for In Vivo Microscopy, Box 3302, Duke University Medical Center, Durham, North Carolina 27710

Ehsan Samei
Duke Advanced Imaging Laboratories (DAI Labs), Departments of Radiology, Physics, and Biomedical Engineering, Medical Physics Graduate Program, Duke University Medical Center, Durham, North Carolina 27710

Cristian T. Badea
Center for In Vivo Microscopy, Box 3302, Duke University Medical Center, Durham, North Carolina 27710

Terry T. Yoshizumi
Department of Radiology and Division of Radiation Safety, Duke University Medical Center, Durham, North Carolina 27710

G. Allan Johnson[a)]
Center for In Vivo Microscopy, Box 3302, Duke University Medical Center, Durham, North Carolina 27710

(Received 16 December 2005; revised 17 August 2006; accepted for publication 18 August 2006; published 20 October 2006)

The increasing use of small animals in basic research has spurred interest in new imaging methodologies. Digital subtraction angiography (DSA) offers a particularly appealing approach to functional imaging in the small animal. This study examines the optimal x-ray, molybdenum (Mo) or tungsten (W) target sources, and technique to produce the highest quality small animal functional subtraction angiograms in terms of contrast and signal-difference-to-noise ratio squared ($SdNR^2$). Two limiting conditions were considered—normalization with respect to dose and normalization against tube loading. Image contrast and $SdNR^2$ were simulated using an established x-ray model. DSA images of live rats were taken at two representative tube potentials for the W and Mo sources. Results show that for small animal DSA, the Mo source provides better contrast. However, with digital detectors, $SdNR^2$ is the more relevant figure of merit. The W source operated at kVps >60 achieved a higher $SdNR^2$. The highest $SdNR^2$ was obtained at voltages above 90 kVp. However, operation at the higher potential results in significantly greater dose and tube load and reduced contrast quantization. A reasonable tradeoff can be achieved at tube potentials at the beginning of the performance plateau, around 70 kVp, where the relative gain in $SdNR^2$ is the greatest. © *2006 American Association of Physicists in Medicine*. [DOI: 10.1118/1.2356646]

Key words: x-ray, digital subtraction angiography, spectra optimization, SNR, contrast, rodent, small animal, functional imaging

I. INTRODUCTION

The increasing use of small animals in basic research has spurred interest in new imaging methodologies—particularly magnetic resonance microscopy, microCT, and microPET.[1–3] Enormous potential exists for functional imaging using micro x-ray given the ease of use and its speed to capture rapid biological changes. Such studies can include measuring pulmonary, renal, or tumor perfusion, cardiac motion, or examining the effects of vascular tonicity-mediated drugs.[4–6]

Functional imaging in small animal models can be addressed particularly well using digital subtraction angiography (DSA). DSA, first suggested by Mistretta *et al.* in the 1970s, is now a routine clinical exam in modern medical centers.[7] Extensive work, ranging from initial engineering studies to evaluating the clinical efficacy, has been done in canines, porcines, and humans.[8–18] Scaling DSA to the higher spatial and temporal resolutions encountered in the rodent presents some particularly interesting opportunities and challenges. Some prior work has been done in mice and rats.[19–24] However, these studies did not address the optimization of radiographic spectra to produce the best contrast and signal-difference-to-noise ratio squared ($SdNR^2$), one of the many components in creating an optimal system designed explicitly for small animal DSA in live rodents. Also, these earlier studies acquired images asynchronous to biological rhythms, such as cardiac or ventilatory cycles, and thus x-ray exposure time was not taken into account. In addition, these studies used significant contrast injection volumes, up to 50% of the mouse total blood volume.

Several scaling differences between mice and humans suggest that a Mo anode might be preferable to the more traditional approach of a W anode used for DSA. The absorption coefficient of I at 17.5–19.7 keV (the *K* emission of Mo) is actually 1.7% higher than the absorption coefficient at the *K* edge (33.2 keV) and 16.6% higher at 35 keV. The absorption coefficient of Gd, the primary phosphor of the

electronic detector used, is significantly higher at 17.5 keV than it is at the iodine *K* edge. Photon production efficiency (flux/mA) is substantially higher for (Mo) *K* emission than it is for W brehmsstrahlung at 17 keV.[25] Finally, since the mouse and rat are quite thin, less than that of a human breast, one might hypothesize that penetration of the low energy $K\alpha$ emission of Mo could provide a superior source for DSA imaging in the mouse. This study explored an optimal DSA technique for live rodent imaging. More specifically, we examined the optimal x-ray source—molybdenum or tungsten—and kVp to produce the highest quality small animal functional subtraction angiograms in terms of contrast-to-noise ratio (CNR) and signal-to-noise ratio (SNR).

II. MATERIALS AND METHODS

This study included both simulation and experimental verification. The three metrics used to determine the optimal x-ray source and technique were contrast, exposure-normalized $SdNR^2$, and tube-load limited $SdNR^2$, defined as

$$\text{Contrast} = \frac{S_{NC} - S_C}{S_{NC}}, \tag{1}$$

and

$$\text{SdNR}^2_{(\log)} = \frac{\left(\log S_{NC}/S_C\right)^2}{\sigma^2\left(1/S_{NC}^2 + 1/S_C^2\right)}, \tag{2}$$

where S_C and S_{NC} are the detector signals with and without contrast agent, respectively. Derivation of the logarithmically subtracted $SdNR^2$ can be seen in the Appendix. The exposure and tube-load limited $SdNR^2$ were expressed in units of $mm^{-2}\,mR^{-1}$ (exposure limited, constant mR) and $mm^{-2}\,mAs^{-1}$ (tube-load limited, maximum mAs output provided by x-ray tubes at each kVp), respectively.

A. Simulation

Image contrast and $SdNR^2$ were simulated using an established x-ray model.[26,27] All simulations were performed using the XSPECT simulation program developed at Henry Ford Health Systems (Detroit, MI). The program uses semiempirical models.[28–33] for generating x-ray spectra. Attenuation from iodinated contrast agent, soft-tissue, and inherent tube filtration was calculated following Beer's law.[34,35] Finally, the resulting spectra was integrated over the energy response function for the Gd phosphor of the phosphor-bound CCD detector employed in the experiments assuming an ideal detector that behaves as a perfect integrator of the energy spectrum. A schematic of the simulation is shown in Fig. 1.

The materials used in the simulation included a 0.045-mm-thick Gd_2O_2S scintillator for the detector; 13- and 30-mm-thick soft-tissue absorbers, simulating the imaging situations for the mouse and rat, respectively; and a 0.28-mm-diam tube with I contrast agent of 37% concentration to represent the major vessels of the mouse and rat.[36,37]

To better reflect the experimental conditions, the simulations included additional Al filtration (2.8 and 0.6 mm for W and Mo, respectively) and a constant scaling factor to match exposure and attenuation measurements from our W and Mo tubes.

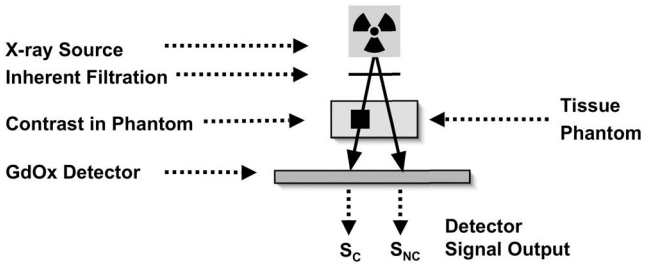

FIG. 1. The schematic shows the x-ray beam path used for the simulations. S_C and S_{NC} are detector signal outputs with and without contrast agent, respectively.

Simulations were performed over a range of tube potentials (18–70 kVp) for x-ray tubes with W and Mo targets. Since the tubes had different focal spot dimensions (0.6 and 1.0 mm for Mo and W, respectively), the data were normalized for source-detector distances that would match the geometric blur of the two tubes.

For clinical imaging, minimization of dose is a major concern. Thus, normalization with respect to exposure is an obvious metric for comparison. For rodent imaging, the higher respiratory and cardiac rates require the exposures to be much shorter than those for humans. At the same time, the higher spatial resolution and statistical considerations require higher exposures to maintain the SNR and CNR. The combination of these two effects suggests an alternative method for normalization against the exposure rate, i.e., normalization with respect to the available flux for a given time and tube loading (Fig. 2). The data analysis included both approaches.

B. Live animal experiment

The radiographic system constructed for this work included an 80 kW generator (Phillips CXP) with a

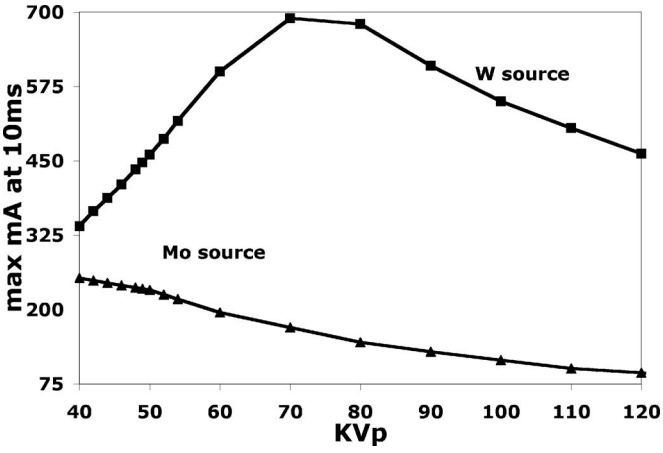

FIG. 2. The maximum current permitted for each tube for a standardized (10 ms) exposure is shown for each tube. Note the much higher currents possible for the W anode.

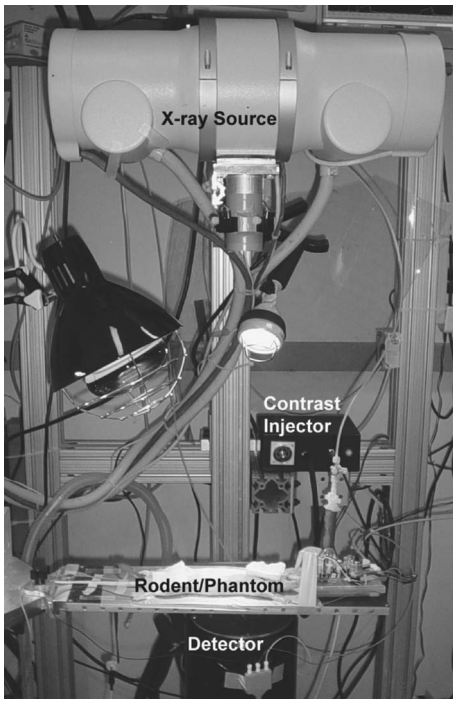

FIG. 3. System during a live animal study.

0.3/1.0 mm focal spot W anode tube and a 65 kW generator (EMD EPS 65RF) with a 0.3/0.6 mm focal spot Mo anode tube. Tubes were mounted on a C-arm constructed from extruded Al. A flexible carbon fiber table designed for rodents floated above a 95×95 mm cooled CCD detector (ImageStar, Photonic Science, East Sussex, England) with a 46×46 μm pitch and a 15 mg/cm^2 ($\sim$45-μm-thick) Gd_2O_2S scintillator. The detector was corrected for gain variations across the field of view. Contrast agent was supplied via a computer-controlled micro-injector. The system was controlled by two computers running custom control software (LabVIEW, National Instruments, Austin, TX) that were linked together to support synchronization of image acquisition with physiologic control.[38] Figure 3 shows the system during a live animal study. X-ray source and detector geometry were adjusted to match penumbral blur to the Nyquist-imposed resolution limit in the detector. Exposures, ventilation, injection, and image capture can be triggered individually to allow a variety of sequences synchronized with physiological parameters.[39]

To provide direct measure of image quality differences in a live rat DSA, images were acquired at 45 and 70 kVp for both anodes under two separate conditions: (1) with the same entrance exposure and (2) with maximum tube loading. In the case of the same entrance exposure imaging, the raw images from the Mo tube were scaled to match the exposure of the W tube because the Mo tube generator had a coarse adjustment in mAs, by 25% steps. We report the relative $SdNR^2$ in the live rodent DSA images of the left pulmonary artery at the same time point in contrast passage. The values were derived experimentally using Eq. (2) where the noise is measured from a ROI in the corner of the image in which there is no structured background. Strictly speaking, this is not the true $SdNR^2$ since the photon flux will be higher in this region than in the region of the anatomical landmark (e.g., pulmonary artery). This method limits any variation between images arising from structure in the object.

Separate animals were used for the images acquired at the same entrance exposure and with maximum tube loading. All animal studies were conducted with approval of the Duke Institutional Animal Care and Use Committee. Right jugular catheters (3F) were placed in female rats (160–190 g, Fischer 344). The animals were anesthetized with Nembutal (50 mg/kg, IP, Abbott Laboratories, North Chicago, IL) and butorphanol (2 mg/kg, IP, Fort Dodge Animal Health, Fort Dodge, IA), perorally intubated, and mechanically ventilated at 60 breaths/min with a tidal volume of 1.5–1.7 mL. Anesthesia was maintained with Isoflurane (1%–3%). Body temperature was measured with a rectal thermocouple and was maintained at constant levels (37 ± 0.1 °C) with a heat lamp controlled via feedback from the thermocouple. Solid-state transducers on the breathing valve measured airway pressure and flow.[40,41] Pediatric electrodes were taped on the footpads for ECG. All physiologic signals were continuously collected (Coulbourn Instruments, Allentown, PA) and displayed on a computer using custom-written software (LabVIEW, National Instruments, Austin, TX) for the duration of the experiment. These signals were also used to control the gating described above. At the conclusion of the studies, the animals were euthanized via an anesthetic overdose.

Radiographic exposures, readout of the camera, and contrast agent injections (Isovue 370, 370 mg iodine/mL, Bracco Diagnostics, Princeton, NJ) were synchronized at the same point in the cardiac cycle with end-respiration apnea. Because the heart rate of a rat is a rapid 450 beats/min, 7.5 times that of a human, the exposure time was kept at $\sim$10 ms to limit motion blur. A micro-injector allowed the control of contrast injection with temporal precision of $\sim$10 ms and volumes down to 6 ± 1 μL. Pulmonary flow could be seen with contrast volumes as low as 1% of the total blood volume in the mouse and at less than 1% of the volume in the rat. Injections were spaced 10 min apart to allow clearance of the contrast agent, which limited complications from background concentrations of contrast in the blood. Separate experiments have been performed with the micro-injector demonstrating reproducibility of the time density curves for a given injection with minimal variations (correlation coefficient $\geqslant 0.9$). Images were logarithmically subtracted[42] and compared.

Dose measurements were made for the maximum tube loading case using MOSFET detectors (mobileMOSFET, LACO, Chesterland, OH). The dosimeter was calibrated using an ionization chamber (Electrometer Model 9015, Probe 10×5-6 was used for the W source, MDH Radcal, Monrovia, CA) with probes sensitive for even at the low Mo energies (Probe 10×5-6-6M-3). The figures reported represent the total integrated dose for a standard DSA study consisting of 30 frames of 10 ms exposures.

III. RESULTS

A. Simulation results

Figure 4 shows the simulation results for contrast, exposure-normalized $SdNR^2$, and image quality normalized $SdNR^2$ for tissue thickness appropriate for our two target applications (i.e., mouse and rat).

Figures 4(a) and 4(b) show that contrast decreases rapidly with increase in tube potential up to the *K* edge of I at 33 keV, where the contrast rises abruptly before falling off again at higher kVps. A rank inversion occurs soon after the *K* edge of the Gd phosphor for mouse and rat. Below the *K* edge of iodine, the source (W or Mo) has a significant impact on contrast. Above the *K* edge, the impact of the anode material is less pronounced.

At constant exposure, the $SdNR^2$ peaks at 20 and 49 kVp for the mouse with both W and Mo sources, Figs. 4(c) and 4(d). The effect of the contrast agent increases the $SdNR^2$ at the *K* edge of iodine as it does for contrast, Figs. 4(a) and 4(b). At the optimum 49 kVp, the $SdNR^2$ is 23.6% (W) and 39.7% (Mo) higher for the rat and mouse imaging situations. At 49 kVp, the $SdNR^2$ is 78.8% (W) and 102% (Mo) greater for the mouse than the rat, and the peak at lower kVp disappears with thicker absorbers (rat).

Figures 4(e) and 4(f) show the $SdNR^2$ normalized against current. With increased tube potential, this metric also increases because the signal, following Poisson statistics, becomes significantly greater than that of noise. Virtually no difference exists between the two anodes for the rat at all kVp. Above 50 kVp, the $SdNR^2$ increases more rapidly for the mouse, reflecting the more efficient *K* production of the Mo anode and its ready penetration of the thinner animal. Following our initial hypothesis, on a per-mAs-basis, the Mo anode is superior to the W anode at all energies for small animal imaging. Note that the rate of increase (slope) is greater for the Mo anode than for the W anode for both mouse and rat.

Figures 4(g) and 4(h) were constructed using the tube loading charts (Fig. 2) available for both of the specific tubes used in this study. Thus, Figs. 4(g) and 4(h) show the $SdNR^2$ at maximum mA for a 10 ms exposure for geometries with equivalent spatial resolution.

The tube-loading chart (Fig. 2) shows an inverted parabola with maximum mAs at 70 kVp. The point-by-point multiplication of the tube-loading chart with Figs. 4(e) and 4(f), results in a steady rise in current limited $SdNR^2$ [Figs. 4(g) and 4(h)] with a plateau at the higher kVps. The rise is more prominent and a plateau at a higher kVp is seen with the W compared to Mo tube. A major contributor to the shape of Figs. 4(g) and 4(h) is the tube loading. As the space charge is overcome, the maximum tube current rises rapidly and then drops off as the thermal limitations of the tube come into play.

There is a dramatic rise in $SdNR^2$ until 80 kVp for rodents, where $SdNR^2$ plateaus for the W anode. The increase in $SdNR^2$ for the Mo tube is more gradual and plateaus at tube potentials above 70 kVp for rodents. The W source is superior at all energies above 60 kVp.

B. Results of live animal experiment

Figure 5 shows logarithmically subtracted DSA images of the rat thorax, taken at the same exposure at 45 and 70 kVp during the same point in the cardiac and respiratory cycle following an injection of 50 μL of Isovue 370 in the right jugular vein. Images were windowed to present comparable displayed contrast.[43] Note the improved visibility of the proximal branching pulmonary arteries in the lungs (dashed arrows) and the increased opacification of the right ventricle (solid arrows) in Fig. 5 with the W tube [Figs. 5(c) and 5(d)] relative to the Mo tube [Figs. 5(a) and 5(b)]. The images taken using the same x-ray source at both tube potentials show similar image quality [Figs. 5(a)–5(d)]. The $SdNR^2 = 49$ for the W source at the low and high tube potentials. $SdNR^2$ values of 41 and 50 were measured for the Mo source operated at 45 and 70 kVp, respectively.

Figure 6 shows logarithmically subtracted images of the rat lung, taken with 10 ms exposure at the maximum mA permissible at 45 kVp [Figs. 6(a) and 6(c)] and 70 kVp [Figs. 6(b) and 6(d)] at the same point in the cardiac and respiratory cycle with a 50 μL injection of Isovue 370 into the right jugular vein. Images were windowed to present comparable displayed contrast as in Ref. 43. The comparison of the relative noise levels and detail in the images confirm simulation results: the Mo x-ray source at the low 45 kVp produces better image quality as seen in Fig. 6(a) than the W source [Fig. 6(c)], while the W x-ray source produces better image quality [Fig. 6(d)] than the Mo source [Fig. 6(b)] at a higher (70 kVp) tube potential. In addition, comparisons of images taken at 45 and 70 kVp with the same x-ray source [Figs. 6(a)–6(d)] show operation at higher kVp to be better in both cases. Note, in particular, the improved visibility of the right ventricular filling (solid arrows) and the distinction between the pulmonary vessels and the lung parenchyma (dashed arrows) in Fig. 6. Quantitative results agree well with the simulations: the W ($SdNR^2 = 144$) and Mo ($SdNR^2 = 81$) x-ray sources at high tube potential (70 kVp) have higher contrast to noise ratio than at lower tube potential (45 kVp) for both the W ($SdNR^2 = 36$) and Mo ($SdNR^2 = 49$) x-ray sources. The dose imparted at the surface was 3.17 cGy (Mo) and 0.99 cGy (W) at 45 kVp, and 4.85 cGy (Mo) and 5.32 cGy (W) at 70 kVp. The f-factor was 0.923 and 0.931 for the W tube at 45 and 70 kVp, respectively, and 0.918 for the Mo tube at both high and low tube potentials.

IV. DISCUSSION

Much work has been done to optimize x-ray spectra for humans by using a variety of x-ray sources, filters, and detectors.[44–50] X-ray spectra for clinical DSA are generally tailored to the 40–80 kVp range, regions B and C in Fig. 7, to exploit the *K* edge of iodine (I). However, the mouse and rat with typical anterior-posterior dimensions of 1.3 and 3 cm, respectively, are well penetrated in region A, below the *K* edge of I, where such studies would not normally be performed. In addition, the attenuation coefficient of I in region A is greater than or equal to the attenuation coefficient in regions B and C. Moreover, the absorption coefficient of the

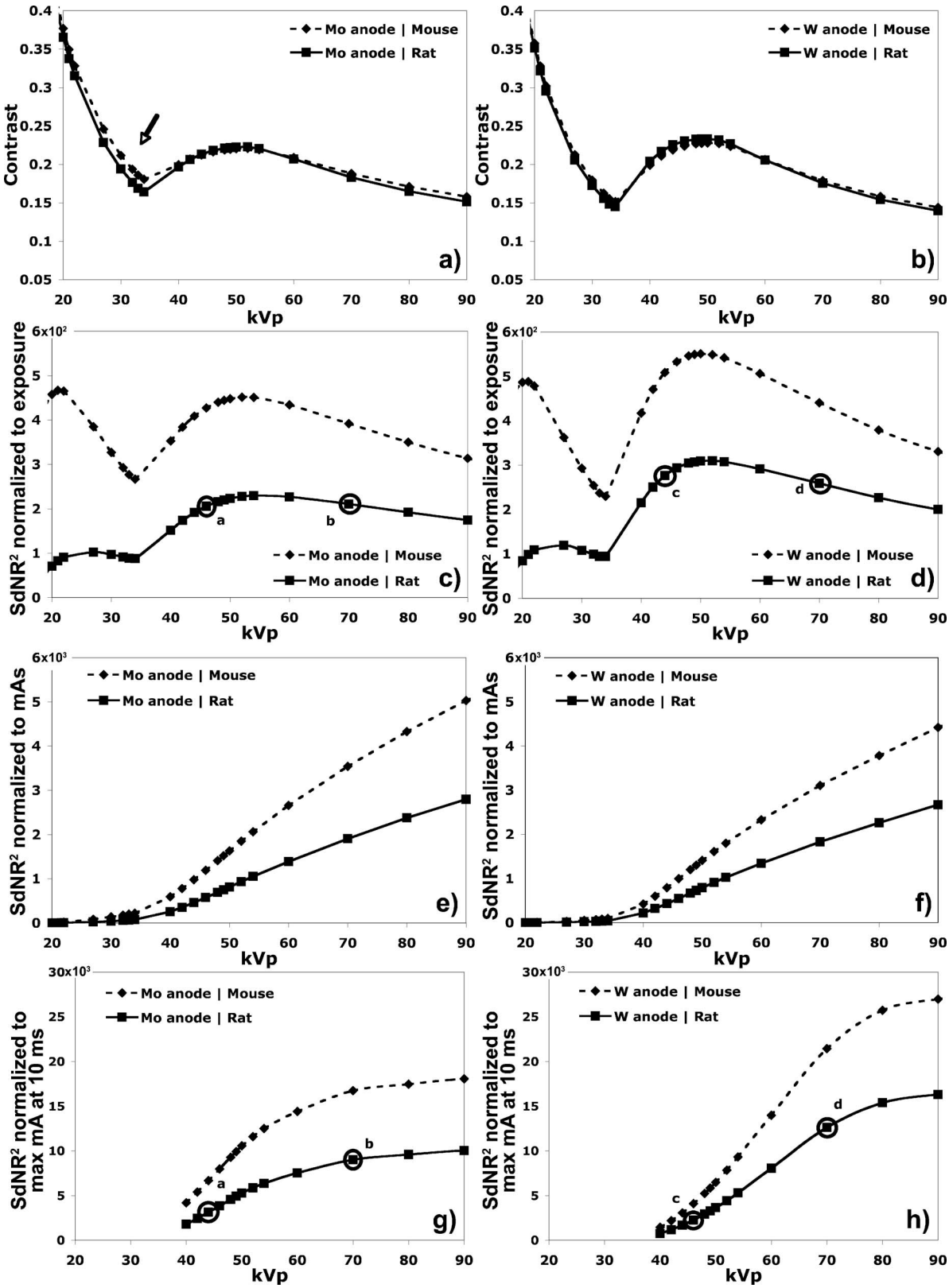

FIG. 4. Contrast vs kVp for Mo (a) and W (b) sources show a much higher contrast for lower kVp as one might expect with the highest contrast for Mo anode in the mouse (arrow). $SdNR^2/(mm^2\ mR)$-normalized to exposure vs kVp for Mo (c) and W (d) sources shows two maxima for the thinner mouse. Lettered regions (a)–(d) within figures correspond to the live rat images shown in Fig. 5. $SdNR^2/(mm^2\ mAs)$ vs kVp for Mo (e) and W (f) sources shows the higher values for the Mo anode for both the mouse and rat at all operating voltages indicating more efficient flux production of the Mo anode. $SdNR^2/mm^2$, at max mA, for a 10 ms exposure vs kVp for Mo (g) and W (h) sources demonstrates superior performance of the W anode. The W source still produces a higher $SdNR^2$ than the Mo source, but only at energies above 60 kVp. Lettered regions correspond to live rat images shown in Fig. 6.

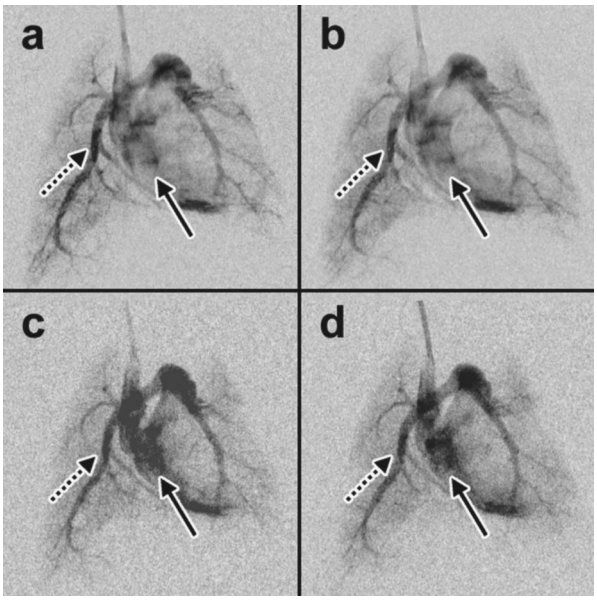

FIG. 5. DSA images of the thorax of a live rat acquired at 45 kVp (a), (c) and 70 kVp (b), (d) at the same exposure using Mo (a), (b) and W (c), (d) anodes. While the Mo anode allows better visualization of distal pulmonary artery branchings, the W anode demonstrates improved visibility of the right ventricle (solid arrow) and proximal pulmonary artery branchings (dashed arrows).

gadolinium (Gd) phosphor is substantially higher in A than in B and C. Our initial hypothesis was that a Mo source, with a 17 keV *K* emission, might take advantage of this higher detection efficiency because of its more efficient flux production at low energies (region A) compared to a W source.[25,51]

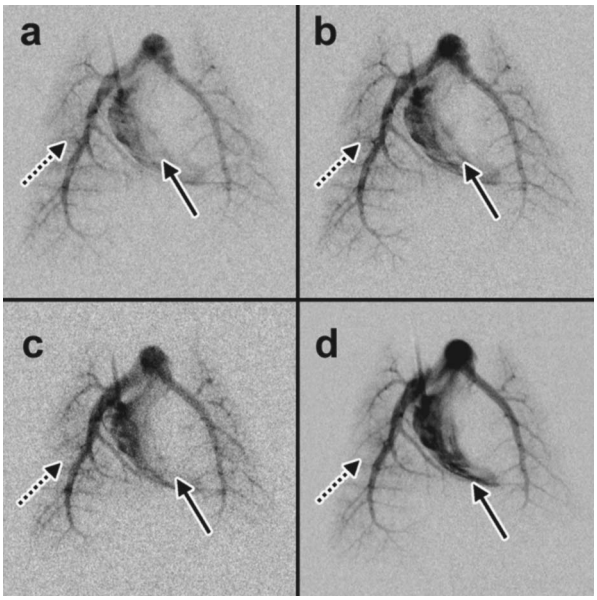

FIG. 6. DSA images of the thorax of a live rat acquired with 10 ms exposure at the maximum mA permissible at 45 kVp (a), (c) and 70 kVp (b), (d) using Mo (a), (b) and W (c), (d). The images demonstrate superior image quality ($SdNR^2$) for the W anode operated at the higher potential. This is seen in the improved visibility of the right ventricular filling (solid arrows) and the ability to distinguish between the lung parenchyma and the pulmonary vessels (dashed arrows).

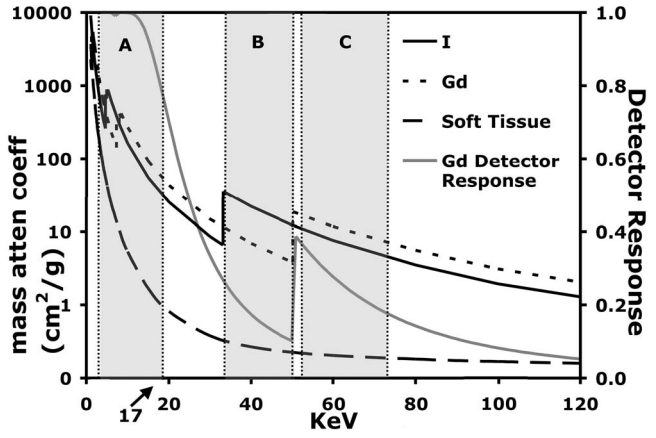

FIG. 7. Attenuation coefficients for I (contrast agent) and Gd_2O_2S (detector phosphor) and detector response curve. Note that in region A, the attenuation coefficient of I is equal to or greater than that in regions B and C. Moreover, the detection efficiency for the Gd phosphor is substantially higher in A than in B and C.

The contrast at lower kVp is marginally higher for the Mo anode. But the more effective metric for DSA is the $SdNR^2$. When normalized to entrance exposure, the $SdNR^2$ is higher for the W anode at all kVp $>$ 33 keV.

Our results have a number of implications in defining the optimal x-ray source and technique to produce the highest quality small animal subtraction angiogram. The effects of varied tube potential and anode material on contrast are consistent with our initial hypothesis and the body of work in mammography. If one corrects for scatter, the thickness of tissue does not have any effect on contrast. Only the thickness of the embedded I contrast agent has an effect on contrast apart from the tissue and contrast agent attenuation:

$$\begin{aligned}\text{Contrast} = \frac{I_{NC} - I_C}{I_{NC}} &= 1 - \frac{I_C}{I_{NC}} \\ &= 1 - \frac{I_0 e^{-\mu_T(T-C)-\mu_C C}}{I_0 e^{-\mu_T T}} \\ &= 1 - e^{(\mu_T-\mu_C)C} \therefore \text{Contrast} \not\propto T. \end{aligned} \quad (3)$$

Here, I_0, I_{NC}, and I_C are entrance, tissue attenuated, and tissue-contrast attenuated x-ray beams, respectively. T and C are the thicknesses, and μ_T and μ_C are the attenuation coefficients of the tissue and embedded contrast. The contrast is higher with the lower energy spectrum of the Mo than the W anode [Figs. 4(a) and 4(b)]. The higher attenuation coefficient of I at lower kVp gives rise to a marked increase in contrast below 26 kVp for both anodes. The *K* edge of I contrast agent at 33 keV causes a steep rise in contrast. As the tube potential is increased, the effective energy of both the Mo and W spectra continue to shift to higher energies above the iodine *K* edge, causing the contrast to drop.

The results for $SdNR^2/(mm^2\ mR)$ versus kVp are shown in Figs. 4(c) and 4(d). As the tissue thickness increases from 1.3 cm (mouse) to 3.0 cm (rat), the peak in the $SdNR^2$ at 20 kVp disappears. The lower energy radiation simply does not adequately penetrate for rat studies. Yet, there remains a

clear optimum kVp for both the mouse and rat at ~50 kVp. The $SdNR^2$ at constant entrance exposure is 23.6% (rat) and 39.7% (mouse) greater for the W anode than Mo anode at this optimal kVp. Images acquired at constant entrance exposure (~20 mR) in Fig. 5 agree well with the simulations; the higher contrast Mo source [Figs. 5(a) and 5(b)] allows better visualization of the distal pulmonary arteries while the proximal branchings of the pulmonary artery and the right ventricle are more apparent in the images acquired with the W [Figs. 5(c) and 5(d)] tube. The pulmonary artery shows more homogeneous enhancement using the W tube (Fig. 5 dashed arrow). Subtle contrast differences seen in the Mo anode [dashed arrow in Fig. 5(a)] are not as apparent with the W anode [dashed arrow in Fig. 5(c)]. Image improvements within the same x-ray source [Figs. 5(a)–5(d)] are not significant. These effects are consistent with the simulation results in Figs. 4(c) and 4(d) and at most a ~20% difference in relative $SdNR^2$.

Figures 4(e) and 4(f) tell a somewhat different story when one takes into account the efficiency of x-ray production. As the accelerating potential increases, the efficiency of photon production increases more rapidly than the contrast decreases resulting in a net increase in $SdNR^2$ as would be expected.[25,52] With this normalization, the Mo anode shows a slightly better performance than the W anode, consistent with our initial hypothesis. But the magnitude of this effect is small. And for the thicker (rat) specimen, there is virtually no benefit for the Mo anode.

Figure 6 demonstrates the most significant practical result from this work. As would be expected, the images clearly improve with higher flux. While flux production is more effective for a given power for the Mo *K* production, the higher heat capacity of the W anode allows operation at significantly higher flux for the short exposures required to limit motion blur. The higher available flux from the W anode at 70 kVp has dramatic impact on our ability to detect the smaller vessels. There was a 78% (70 kVp) and 294% (45 kVp) improvement in relative $SdNR^2$ for the Mo source, and a 400% improvement for the W source operated at 45 kVp. While the dose is relatively high (5.32 cGy) at the surface, it is significantly less than what a typical commercial microCT scanner would impart and at most 1/100 of the LD50/30 of a mouse,[53] thus allowing sequential studies with confidence of little x-ray-induced damage to the small animal.

V. CONCLUSION

Our initial hypothesis predicted the utility of a Mo anode tube for DSA studies in the rodent based upon more efficient flux production from the *K* emission and increased absorption for both I contrast and Gd phosphor at the Mo *K* emission. The simulations demonstrated improved contrast for the Mo anode, but the use of a more appropriate image quality metric, i.e., the $SdNR^2$, showed marginal value for the Mo anode. The need for very short (10 ms) exposures in small animal imaging places a premium on very high photon flux, which can be more effectively obtained from a W anode operating at ~70 kVp.

The use of DSA for small animal imaging has been limited to date. The success of MR microscopy in the 1980s and 1990s, and the more recent development of CT, PET, and SPECT systems scaled for small animals have focused the attention of researchers away from the simpler radiographic method. But the development of high-resolution cooled CCD detectors, physiologic monitoring and control methods for small animals,[38,54] computer-controlled injection as performed in this work, and the integration of all of these elements into an operational platform designed for small animals promise some exciting new imaging alternatives for functional vascular imaging not possible with existing small animal imaging systems. The DSA system described here can acquire projection images covering an entire rat or mouse with an effective time sample of 10 ms at frame rates (7–10 fps) far beyond any of the other modalities and 2D projected spatial resolution $<100\ \mu$m. What we know to be true in the clinical domain, i.e., that each of our modern modalities has utility driven by the clinical problem, is also true at the level of the small animal. We believe small animal DSA will play a major role in functional vascular phenotyping.

ACKNOWLEDGMENTS

The authors wish to thank Michael Flynn for XSPECT, Greta Toncheva and Giao Nguyen for assistance in dosimetry measurements, Jim Pollaro for the ventilator software control interface and monitoring system, Julie Boslego Mackel, Boma Fubara, and Laurence Hedlund for animal support and surgery, and Lutao Ning for help with the micro-injector. All work was performed at the Duke Center for In Vivo Microscopy, an NCRR/NCI National Biomedical Technology Resource Center (P41 RR005959, R24 CA 092656).

APPENDIX

The logarithmic subtraction signal difference and noise characteristics of this study can be written as

$$S_{d(\log)} = \log(aE_0 + b) - \log(aE_I + b)$$

$$\text{assuming no offset or } b = 0$$

$$S_{d(\log)} = \log E_0 - \log E_I,$$

where E_I and E_0 are exposures with and without contrast agent, respectively.

The form $aE+b$ uses a linear relationship of exposure to the gain (a) and offset (b) of the detector pixel value,

$$\sigma^2_{S_d(\log)} = \left(\frac{\sigma_{E_0}}{E_0}\right)^2 + \left(\frac{\sigma_{E_I}}{E_I}\right)^2 \quad \text{assuming } \sigma_{E_0} = \sigma_{E_I}$$

$$= \sigma^2_{E_0}\left(\frac{1}{E_0^2} + \frac{1}{E_I^2}\right) = \frac{\sigma^2_{E_0}}{E_0^2}\left(\frac{1}{(1-C)^2} + 1\right),$$

where

$$C = \frac{E_0 - E_I}{E_0}.$$

Thus, the noise contribution from logarithmic subtraction is related to the noncontrast exposure signal and the radiographic contrast, C. The SdNR^2 of logarithmic subtraction is expressed as

$$\mathrm{SdNR}^2_{(\log)} = \frac{\left(\log E_0/E_I\right)^2}{\sigma^2_{E_0}\left(1/E_0^2 + 1/E_I^2\right)} = \frac{2\log E_0/E_I}{\sigma^2_{E_0}/E_0^2\left(1/(1-C)^2 + 1\right)},$$

where

$$C = \frac{E_0 - E_I}{E_0}.$$

[a]Electronic mail: gaj@orion.duhs.duke.edu

[1]P. L. Chow, F. R. Rannou, and A. F. Chatziioannou, "Attenuation correction for small animal PET tomographs," Phys. Med. Biol. **50**, 1837–1850 (2005).
[2]A. A. Ali *et al.*, "Automated segmentation of neuroanatomical structures in multispectral MR microscopy of the mouse brain," Neuroimage **27**, 425–435 (2005).
[3]C. Badea *et al.*, "4D micro-CT of the mouse heart," Mol. Imaging **4**, 110–116 (2005).
[4]C. T. Badea *et al.*, presented at the IEEE International Symposium on Biomedical Imaging: From Nano to Macro, Arlington, VA, 2006 (unpublished).
[5]M. Lin, L. W. Hedlund, and G. A. Johnson, presented at the IEEE International Symposium on Biomedical Imaging: From Nano to Macro, Arlington, VA, 2006 (unpublished).
[6]N. Mistry *et al.*, presented at the IEEE International Symposium on Biomedical Imaging: From Nano to Macro, Arlington, VA, 2006 (unpublished).
[7]C. Mistretta *et al.*, "Multiple image subtraction technique for enhancing low contrast periodic objects," Invest. Radiol. **8**, 43–49 (1973).
[8]C. B. Higgins, "Quantitation of left ventricular dimensions and function by digital video subtraction angiography," Curr. Probl Diagn. Radiol. **144**, 461–469 (1982).
[9]C. B. Higgins and E. Buonocore, "Digital subtraction angiography. Techniques and applications for evaluating cardiac anatomy and function," Cardiol. Clin. **1**, 413–425 (1983).
[10]F. H. Burbank, "AUR Memorial Award. Determinants of contrast enhancement for intravenous digital subtraction angiography," Invest. Radiol. **18**, 308–316 (1983).
[11]K. Velkova, "Digital subtraction angiopulmography in children," Folia Med. (Plovdiv) **34**, 37–40 (1992).
[12]D. L. Rubin *et al.*, "An experimental evaluation of central vs peripheral injection for intravenous digital subtraction angiography (IV-DSA)," Invest. Radiol. **19**, 30–35 (1984).
[13]T. Meaney, "Digital subtraction angiography of the human cardiovascular system," AJR, Am. J. Roentgenol. **135**, 1153–1160 (1980).
[14]F. J. Schlueter *et al.*, "Digital subtraction versus film-screen angiography for detecting acute pulmonary emboli: Evaluation in a porcine model," J. Vasc. Interv Radiol. **8**, 1015–1024 (1997).
[15]J. Ludwig *et al.*, 'Digital subtraction angiography of the pulmonary arteries for the diagnosis of pulmonary embolism," Radiology **147**, 639–645 (1983).
[16]M. Kalinowski *et al.*, "X-ray digital subtraction angiography with 1 mol/L gadobutrol: Results from a comparative porcine study with iodinated contrast agents," Invest. Radiol. **37**, 254–262 (2002).
[17]M. Hirata *et al.*, "Computational imaging of cerebral perfusion by real time processing of DSA images. Clinical applications," Neurol. Res. **20**, 327–332 (1998).
[18]A. Crummy, "Computerized fluoroscopy: Digital subtraction for intravenous angiocardiography and arteriography," AJR, Am. J. Roentgenol. **135**, 1131–1140 (1980).
[19]V. Bhargava *et al.*, "Systolic and diastolic global right and left ventricular function assessment in small animals using an automated angiographic technique," IEEE Comput. Cardiol. 191–194 (1992).
[20]S. Ono *et al.*, "In vivo assessment of left ventricular remodeling after myocardial infarction by digital video contrast angiography in the rat," Curr. Sci. **28**, 349–357 (1994).
[21]H. A. Rockman *et al.*, "Molecular and physiological alterations in murine ventricular dysfunction," Proc. Natl. Acad. Sci. U.S.A. **91**, 2694–2698 (1994).
[22]F. Ouandji *et al.*, "Characterization of a CCD-based digital x-ray imaging system for small-animal studies: Properties of spatial resolution," Appl. Opt. **41**, 2420–2427 (2002).
[23]S. Kobayashi *et al.*, "In vivo real-time microangiography of the liver in mice using synchrotron radiation," J. Hepatol **40**, 405–408 (2004).
[24]M. Longo *et al.*, "Cerebral angiography in the rat with mammographic equipment: A simple cost-effective method for assessing vasospasm in experimental subarachnoid haemorrhage," Neuroradiology **44**, 689–694 (2002).
[25]G. Johnson and F. O'Foghludha, "Simulation of mammographic X-ray spectra," Med. Phys. **7**, 189–195 (1980).
[26]R. McKinley *et al.*, "Simulation study of a quasi-monochromatic beam of x-ray computed mammography," Med. Phys. **31**, 800–813 (2004).
[27]E. Samei and M. J. Flynn, "An experimental comparison of detector performance for computed radiography systems," Med. Phys. **29**, 447–459 (2002).
[28]T. Fewell, R. Shuping, and K. Hawkins, *Handbook of Computed Tomography X-ray Spectra* (USGPO, Washington, DC, 1981).
[29]M. Szulc and P. Judy, "Effect of x-ray source filtration on dose and image performance on CT scanners," Med. Phys. **6**, 479–486 (1979).
[30]E. Storm, "Calculated bremsstrahlung spectra from thick tungsten targets," Phys. Rev. A **5**, 2328–2338 (1978).
[31]T. Fewell and R. Shuping, *Handbook of Mammographic X-ray Spectra* (USGPO, Washington, DC, 1978).
[32]T. Tabata, R. Ito, and S. Okabe, "Generalized semiempirical equations for the extrapolated range of electrons," Nucl. Instrum. Methods **103**, 85–91 (1972).
[33]E. Storm, "Emission of characteristic L and K radiation from thick tungsten targets," J. Appl. Phys. **43**, 2790–2796 (1972).
[34]H. E. Johns and J. R. Cunningham, *The Physics of Radiology*, 3rd ed. (Thomas, Springfield, IL, 1974).
[35]W. McMaster *et al.*, "Compilation of x-ray cross-sections, Lawrence Radiation Laboratory Report, in UCRL-50174," Springfield, VA, 1969.
[36]K. Chootip *et al.*, "Regional variation in P2 receptor expression in the rat pulmonary arterial circulation," Br. J. Pharmacol. **137**, 637–646 (2002).
[37]H. C. Champion *et al.*, "In vivo gene transfer of prepro-calcitonin gene-related peptide to the lung attenuates chronic hypoxia-induced pulmonary hypertension in the mouse," Circulation **101**, 923–930 (2000).
[38]C. T. Badea, L. W. Hedlund, and G. A. Johnson, "Micro-CT with respiratory and cardiac gating," Med. Phys. **31**, 3324–3329 (2004).
[39]M. Lin, C. T. Badea, and G. A. Johnson, presented at the Academy of Molecular Imaging Annual Conference, Orlando, FL, 2005 (unpublished).
[40]B. T. Chen, A. C. S. Brau, and G. A. Johnson, "Measurement of regional lung function in rats using hyperpolarized 3Helium dynamic MRI," Magn. Reson. Med. **49**, 78–88 (2003).
[41]B. T. Chen, A. T. Yordanov, and G. A. Johnson, "Ventilation-synchronous MR microscopy of pulmonary structure and ventilation in mice," Magn. Reson. Med. **53**, 69–75 (2005).
[42]S. Balter *et al.*, "Digital subtraction angiography: Fundamental noise characteristics," Radiology **152**, 195–198 (1984).
[43]E. Samei *et al.*, "A framework for optimizing the radiographic technique in digital x-ray imaging," Radiation Protection Dosimetry **114**, 220–229 (2005).
[44]M. A. Whall, "Optimization of x-ray spectra for mammography," Br. J. Radiol. **66**, 384–385 (1993).
[45]J. V. Cook *et al.*, "Key factors in the optimization of paediatric x-ray practice," Br. J. Radiol. **74**, 1032–1040 (2001).
[46]M. Sandborg *et al.*, "Schemes for the optimization of chest radiography using a computer model of the patient and x-ray imaging system," Med. Phys. **28**, 2007–2019 (2001).

[47]O. W. Hamer *et al.*, "Contrast-detail phantom study for x-ray spectrum optimization regarding chest radiography using a cesium iodide-amorphous silicon flat-panel detector," Invest. Radiol. **39**, 610–618 (2004).
[48]G. McVey *et al.*, "A study and optimization of lumbar spine x-ray imaging systems," Br. J. Radiol. **76**, 177–188 (2003).
[49]J. T. Dobbins III *et al.*, "Chest radiography: Optimization of x-ray spectrum for cesium iodide-amorphous silicon flat-panel detector," Radiology **226**, 221–230 (2003).
[50]N. N. Blinov, E. B. Kozlovsky, and B. I. Leonov, "Optimization of x-ray mammography conditions," Med. Prog. Technol. **18**, 69–72 (1992).
[51]G. A. Johnson and F. O'Foghludha, "An experimental 'trans-molybdenum' Tube for Mammography," Radiology **12**, 511–516 (1978).
[52]R. A. Kruger and S. J. Riederer, *Basic Concepts of Digital Subtraction Angiography* (Hall, Boston, MA, 1984).
[53]N. L. Ford, M. M. Thornton, and D. W. Holdsworth, "Fundamental image quality limits for microcomputed tomography in small animals," Med. Phys. **30**, 2869–2877 (2003).
[54]W. Mai *et al.*, "Effects of breathing and cardiac motion on the spatial resolution in microscopic imaging of rodents," Magn. Reson. Med. **53**, 858–865 (2005).